Mode localization transition in ferromagnetic microscopic rings

F. Giesen,[1,2,3,*] J. Podbielski,[1] and D. Grundler[4,†]

[1]*Institut für Angewandte Physik und Mikrostrukturforschungszentrum, Universität Hamburg, Jungiusstraße 11, 20355 Hamburg, Germany*

[2]*Department of Physics, University of Alberta, Edmonton T6G 2J1, Alberta, Canada*

[3]*Max-Born-Institut für Nichtlineare Optik und Kurzzeitspektroskopie, Max-Born-Straße 2A, 12489 Berlin, Germany*

[4]*Department E10, Fakultät für Physik, TU München, James-Franck-Straße 1, 85747 Garching, Germany*

(Received 13 February 2007; revised manuscript received 30 April 2007; published 26 July 2007)

We present a combined experimental, computational, and semianalytical study of the magnetization dynamics of permalloy disks and nanostructured rings with a systematically varied ring width. We investigate the dynamics of the quasisaturated state. In the case of wide rings the spin wave mode spectrum is similar to that of a disk. The small inner hole can be viewed as a weak perturbation. When the central hole increases, its influence becomes more important and two characteristic modes form gradually. They become localized at different positions in the ring. We explain the localization by the increasing inhomogeneity of the internal magnetic field and the formation of domain wall regions as the rings grow more narrow. In narrow rings one of the modes is clearly confined to the two segments where the internal field H_{int} is at a maximum and the other to the domain wall region where H_{int} is small. Dynamic magnetic simulations agree well with the measured spectra and confirm this interpretation. We also applied a semianalytical model, which confirms that the mode localization is driven by the internal field inhomogeneity.

DOI: 10.1103/PhysRevB.76.014431 PACS number(s): 75.40.Gb, 75.75.+a, 76.50.+g, 75.30.Ds

I. INTRODUCTION

There is an ongoing research of the spin wave mode spectrum in small confining geometries.[1–17] The motivation is driven by both technological applications and scientific interest. The application of bit patterned magnetic recording media requires a thorough understanding of the spin-wave mode spectrum of nanomagnets to engineer fast reversal speeds,[18–24] minimize noise,[25] and provide high stability against unintended switching.[26–29] Magnetic rings are among the candidates for such applications as they display a stable flux-closure state with vanishing stray field.[30,31] The dynamics of this so-called vortex state has recently been addressed experimentally by different groups.[10,32] Switching the circulation direction in a deterministic way might however involve the transient formation of the polarized onion state.[33]

Scientific interest originates from the prospect of understanding magnetic excitations in confined geometries. The lateral dimensions of magnetic elements can readily be fabricated to have dimensions similar to wavelengths of magnetostatic spin waves. The mode spectrum has been found to depend on the device geometry and to exhibit discrete eigenfrequencies.[6,33–35] In addition spin waves are a type of waves with inherently anisotropic dispersion[36,37] and a low nonlinearity threshold.[38] They display a range of fascinating phenomena such as room-temperature Bose-Einstein condensation[39] or soliton formation.[16]

Even in the linear regime the spectrum of spin waves can become complicated if the symmetry of the confining geometry is low. An example is given by a rectangular magnetic element which exhibits triangular domains in the flux-closure state. Here, the spectrum consists of a quasicontinuum of spin waves.[40] Even in simple device geometries the spatial profile of the internal field H_{int} is in general inhomogeneous. As H_{int} is the determining factor the spin wave spectrum analysis is complicated and often only feasible if one uses computational micromagnetics. Therefore studying well-defined device geometries and internal field profiles is a helpful basis to understand spin dynamics in more complicated cases. Spin wave dynamics for the onion state of permalloy[8,9] and Co rings[11] have recently been reported.

We investigated the spin wave mode spectrum of magnetic permalloy ($Ni_{80}Fe_{20}$) disks and rings. The ring widths were varied systematically between $w=300$ and 930 nm. Broadband spin dynamics measurements were performed in the quasisaturated state. Applying the same external in-plane field H_{ext} the different geometrical parameters varied the spatial profile of H_{int}. The experiments and computational results show that the spin wave eigenmodes become more and more localized when we decrease the width w. The localization occurs due to the field inhomogeneity: modes are localized either at the maximum of the internal magnetic field or in the domain wall regions, where H_{int} is minimal. Starting from the localized character of the eigenmodes at small w we developed a semianalytical description, which helps to (i) model the measured spin wave eigenfrequencies without time-consuming micromagnetic simulations, (ii) illustrate in detail the microscopic process of localization, and (iii) classify the spin waves. A similar approach has recently turned out to be powerful to explain the nature of spin waves in the vortex state in rings.[10] In this paper we focus on the quasisaturated state.

The paper is organized as follows. We give an introduction to experimental and computational details in Sec. II. The experimental and computational results are presented in Sec. III. In Sec. IV we discuss the microscopic process of the mode localization transition, first qualitatively in Sec. IV A then with a semianalytical approach in the following Secs. IV B and IV C. Our conclusions are presented in Sec. V.

II. BASICS OF EXPERIMENT AND SIMULATION

We investigated arrays consisting of 750 nanostructured disks or concentric rings. Within each array the rings were

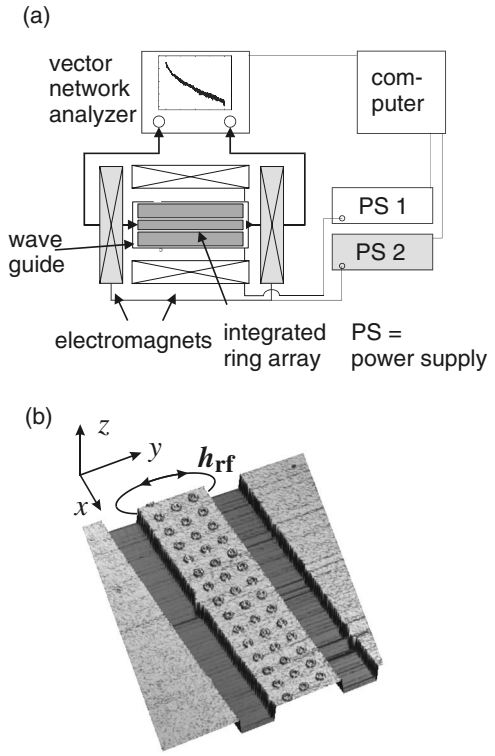

FIG. 1. (a) Schematics of the broadband spin wave spectrometer based on a vector network analyzer and a coplanar wave guide (CPW). A magnetic field H_{ext} may be generated by two orthogonal electromagnets at any in-plane direction. (b) Atomic force micrograph of a CPW with an integrated ring array on the central conductor having a width of 15 μm. The coordinate system used throughout the paper is shown. The ellipse illustrates the approximate shape of the excitation field.

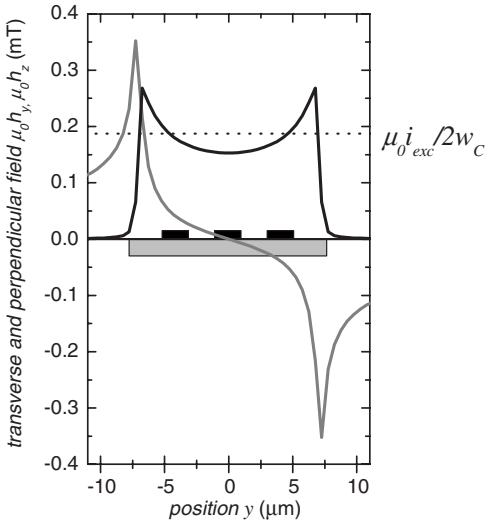

FIG. 2. Magnetic excitation fields 100 nm above the center conductor of the CPW calculated according to Biot-Savart's law (Ref. 41) with a realistic current density. The black and grey lines are the in-plane and out-of-plane fields, respectively. The sketched inset shows the cross section of the center conductor (grey rectangle) and the ring rows (black rectangles) to scale. The dashed line indicates the level of the magnetic field for a fictitious constant current density.

nominally identical and had a constant width w. The ring widths were varied systematically from array to array. Devices were prepared by electron beam lithography and subsequent lift off. The magnetic material was thermally evaporated permalloy. All rings in this study had a thickness of $t=14$ nm as measured by atomic force microscopy. The rings had an outer diameter of $D_0=2$ μm and a center to center spacing of 4 μm to minimize coupling between the rings. The ring arrays were incorporated on a coplanar waveguide structure (CPW) on a GaAs substrate. The center conductor was used for the excitation of the magnetization dynamics and its inductive detection. A sketch of the setup and an atomic force micrograph of a part of the central conductor with integrated ring array are shown in Fig. 1. The CPW was optimized to exhibit an impedance Z_0 close to 50 Ω. To apply the excitation current and to detect the absorption of the rings we connected the CPW with high bandwidth probes to a vector network analyzer in transmission geometry. The bandwidth of our setup is 45 MHz to 20 GHz. Static magnetic fields of up to $\mu_0 H_{ext}=100$ mT were applied in the plane of the ring arrays.

In the setup a sinusoidal high frequency current is passed through the waveguide and produces a corresponding magnetic field. Since the waveguide supports quasi-TEM modes the field component in the propagation direction is negligible $h_x \ll (h_y, h_z)$. If the current density were uniform over the conductor the field would lie almost perfectly in the plane of the rings and perpendicular to the direction of the waveguide. In this case an analytical expression for the magnetic field is given by $\mu_0 h_{rf}=\mu_0 i_{exc}/2w_C$.[42–44] Here, i_{exc} is the excitation current through the waveguide and $w_C=15$ μm is the width of the central conductor. At GHz frequencies the current is pushed toward the conductor edges due to the self-inductance of the conductor.[41] We have used free commercial software[45] to calculate the current density distribution in the CPW at 20 GHz.[46] From this distribution we calculate the excitation magnetic field profile using the Biot and Savart law. The result is shown in Fig. 2. The in-plane component of the field h_y over the central conductor is almost constant across the rings but grows larger towards the conductor edges. The fact that the outer ring rows are subject to a slightly stronger in-plane field component should not play an important role as long as the excitation field strength is small and in the linear regime of spin wave dynamics. The horizontal line indicates the analytically expected value assuming a homogeneous current density. This constant value becomes true in the dc limit, and is a good approximation for frequencies in the low MHz range. The out-of-plane field has a high absolute value only at the edges outside the ring rows. The inhomogeneity should therefore play a minor role. To substantiate this assumption we have performed some micromagnetic simulations with both, a realistic excitation field profile and a fictitious homogeneous excitation field. We have not detected a difference in the calculated spectra.

The magnetic response of the rings $\boldsymbol{m}(\omega,t)=\hat{\chi}(\omega)\boldsymbol{h}_{rf}(\omega,t)$ induces a voltage in the waveguide, which after Ref. 42 is calculated from reciprocity as

$$V_{\mathrm{ind}} = \frac{\mu_0 N}{2} \int_{\mathrm{ring}} \tilde{\boldsymbol{h}} \frac{d\boldsymbol{m}(\boldsymbol{r},t)}{dt} d^3 r. \quad (1)$$

This voltage is picked up by the waveguide. Here, $\hat{\chi}$ is the tensor of the complex magnetic susceptibility, and the integration extends over the whole ring. N is the number of rings in each array. $\tilde{\boldsymbol{h}}$ is the magnetic field per unit current of the CPW and reflects the spatial profile of the excitation magnetic field $\boldsymbol{h}_{\mathrm{rf}}$. Equation (1) shows that due to the excitation field profile only the transverse component of the dynamic magnetization $\boldsymbol{m}_t=(m_y,m_z)$ is excited and detected. Roughly speaking, the ratio of in- and out-of-plane components m_z/m_y is similar to the small aspect ratio $t/D_0 \ll 1$. Therefore the detected signal is dominated by m_y. When the dynamic magnetization is at resonance the phase shift between the excitation current and the induced current $i_{\mathrm{ind}}=Z_0 V_{\mathrm{ind}}$ is π (destructive superposition) and absorption peaks occur at the eigenmodes of the rings. At resonance, the shift between magnetization $\boldsymbol{m}$ and excitation magnetic field $\boldsymbol{h}_{\mathrm{rf}}$ is $\pi/2$ because then the real part of the susceptibility is zero. Due to the derivative in Eq. (1) there is an additional phase shift of $\pi/2$ adding to a total phase difference of π between i_{ind} and i_{exc}.

To detect only those changes in the transmission signal caused by the absorption due to spin waves in the rings, traces are measured with the ring magnetization saturated perpendicularly to the wave guide (reference) and along the wave guide.[8,42,43,47] In perpendicular saturation, excitation and detection of magnetization dynamics are vanishingly small because (i) the torque on the static magnetization is tiny, i.e., $\tau=\boldsymbol{h}_{\mathrm{rf}}\times\boldsymbol{M}\approx 0$ and (ii) in this perpendicular configuration the dynamic magnetization is oriented such that the induced voltage is very small, given mainly by the out-of-plane precessional component m_z, i.e., $\boldsymbol{h}_{\mathrm{rf}}\cdot d\boldsymbol{m}/dt \approx i\omega h_z m_z \approx 0$. This holds because at the position of the rings $\boldsymbol{h}_{\mathrm{rf}}$ is mainly in the plane of the CPW [see Fig. 2 and Eq. (1)]. Therefore, in the perpendicular saturation we measure a reference absorption spectrum where absorption features due to spin waves are at a minimum or even absent. This reference spectrum is subtracted from the data taken at $\mu_0 H_{\mathrm{ext}}=90$ mT applied along the CPW's central conductor, and the difference spectrum then displays spin wave absorption peaks with an optimized signal-to-noise ratio.

To interpret the measured eigenmode spectra of the rings we performed micromagnetic simulations with the LLG code[48] and a semianalytical calculation. Combining the two approaches later is instructive to clarify the microscopic mechanism underlying the mode localization. For the LLG code a single ring was discretized in a mesh with $400\times400\times2$ cells ($5\times5\times7.25$ nm^3). The geometrical ring parameters were taken from scanning electron microscopy and atomic force microscopy. The gyromagnetic ratio was $\gamma=28$ GHz/T, the saturation magnetization $\mu_0 M_S=1.36$ T, both determined from a witness sample deposited in the same deposition step as the rings. The exchange constant A was 1.05×10^{-11} J/m. The damping constant α was chosen to be 0.01. This value was chosen about ten percent higher than determined from a witness film. By taking this larger value we intended to mimic the FMR linewidth obtained on an array where besides the intrinsic damping also array inhomogeneities might provoke a broadening of resonances (e.g., due to variations in ring widths or local oxidation of inner and outer edges that are not present in the witness film). As will be seen later, the simulation parameters provide consistent spectra for almost all the different arrays investigated in the experiments. Only for rings with $w=930$ nm the damping is overestimated such that a satellite mode might be merged with the main mode. We used free boundary conditions. Based on these data we simulated the equilibrium magnetic configuration at 90 mT. These equilibrium states were used as the initial state for the dynamics simulations. To evaluate frequencies up to 40 GHz the Landau-Lifshitz-Gilbert equation was integrated with time steps of 0.25 ps and for a time duration of 7 ns. The time evolution of each cell $\boldsymbol{m}(x_n,y_n,z_n,t)$ was recorded after a delta-pulse type of excitation $\boldsymbol{h}_{\mathrm{rf}}(t)=h_0\delta(t)\hat{\boldsymbol{e}}_y$ with $\mu_0 h_0=0.3$ mT. This value is slightly higher than that calculated from the power of the VNA output and the CPW geometry but it shows that we are well within the linear regime. Then we performed a fast Fourier transformation and plotted the spectral amplitude at a given frequency for each cell. Thereby the eigenmodes of the rings were visualized. The experimentally measured quantity, the induced voltage V_{ind}, is proportional to the susceptibility weighted by the frequency. Therefore, to compare the simulated and measured spectra, the simulations were also weighted by the frequency.[49] Spatial profiles of the static internal field were separately simulated using the free OOMMF code[50] with a 2D solver but otherwise identical simulation parameters. Comparisons between OOMMF and LLG solver revealed nearly identical magnetization states. Results for the equilibrium magnetizations are shown in Fig. 3. For all ring widths we find the quasi-saturated state with both ring arms magnetized in parallel.

To clarify in detail the localization process we adapted a semi-analytical calculation and interpreted the data on the basis of a WKB-like approximation. The model is presented in detail in Sec. IV. This model highlights the physics behind mode localization in rings.

III. EXPERIMENTAL AND COMPUTATIONAL RESULTS

A. Experimental results

In Fig. 4 we present absorption spectra of the investigated arrays at 90 mT. This external field generates the quasi-saturated state (Fig. 3) in all samples. For disks [Fig. 4(a)], i.e., a hole diameter of zero, we observe a very dominant mode, labeled B, at 9.9 GHz. There are several higher and lower modes but with substantially smaller absorption strength in the spectrum. The frequency of the main mode B is slightly smaller than the uniform mode of the unpatterned permalloy film at the same magnetic field. In the presence of a small hole of 140 nm diameter, i.e., $w=930$ nm, satellite modes (labeled A) appear at the high frequency side of the main absorption peak B [Fig. 4(b)]. The dominant mode B is shifted to a lower frequency. For the rings with $w=830$ nm [Fig. 4(c)] the splitting $\Delta f_{AB}=f_A-f_B$ between modes B and A

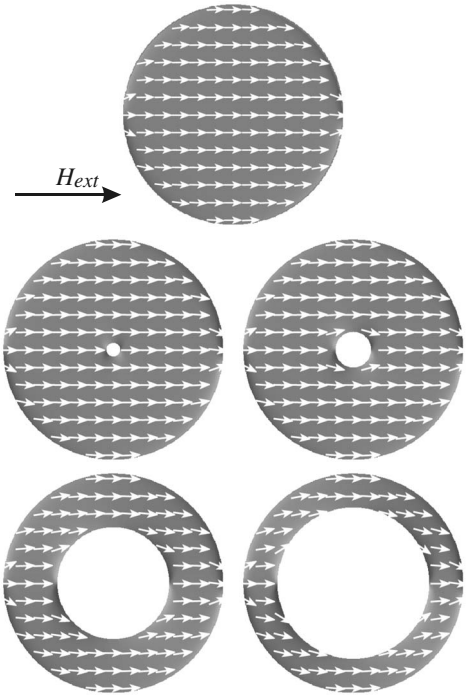

FIG. 3. Computational magnetization configuration for the disk and rings at $\mu_0 H_{\text{ext}}=90$ mT. The calculation was performed with geometrical parameters from AFM measurements and magnetic parameters from measurements on a witness sample. For all ring widths we find the quasisaturated state with the magnetization in the ring arms in parallel.

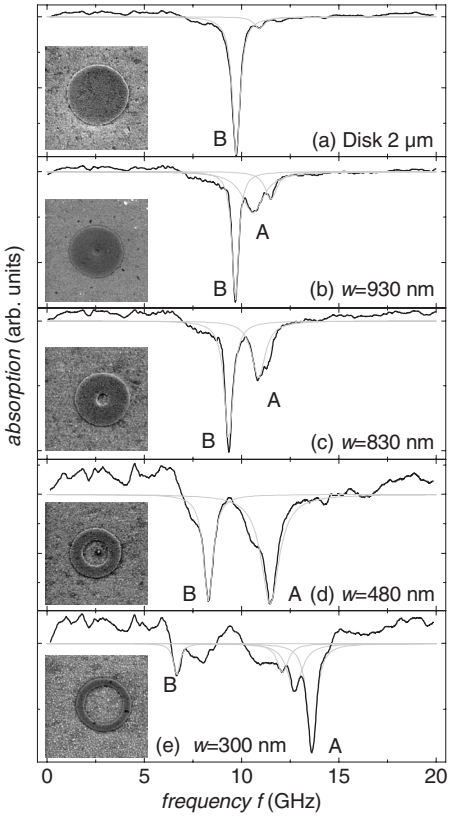

FIG. 4. Measured absorption spectra of disks and rings at $\mu_0 H_{\text{ext}}=90$ mT. The rings had different widths (listed in the panels). The insets show scanning electron micrographs of an individual ring from each array.

becomes more pronounced. The relative absorption strength $\eta_{AB}=p_A/p_B$, where p_A and p_B are the absorbed power in the respective mode, grows larger than in the disk sample. At a ring width of 480 nm [Fig. 4(d)] the absorption strengths of mode A and B are equal, i.e., $\eta_{AB}\sim 1$ and their splitting has further increased. Additional satellites appear as shoulders on the low-frequency side of both modes A and B. For the narrowest rings [Fig. 4(e)] mode A is the dominant mode ($\eta_{AB}>1$) and the splitting is largest. In addition to the main peaks two satellites are seen clearly below mode A for rings with $w=300$ nm.

We note that the characteristic features of the mode spectrum remain similar throughout the magnetic field regime where the rings are in the onion state (not shown). With decreasing external magnetic field the peaks are found to shift to lower and lower frequencies as expected (see Refs. 8 and 11). Some of the satellite peaks disappear at fields slightly higher than the switching field at the transition from the onion to the vortex state. Summarizing the experimental data, we observe prominent absorption peaks which are caused by the spin-wave eigenmodes of disks and rings. There is a systematic development of the modes as a function of the hole diameter.

B. Computational micromagnetics results

Computational micromagnetics spectra are displayed in Figs. 5(a)–5(e). The eigenfrequencies of the modes A and B, their relative absorption strengths, and the presence of pronounced satellite modes are in good agreement with our experimental observations. With increasing hole diameter, starting from the disk and going to the narrowest rings, the simulations reproduce the appearance and systematic development of the frequency splitting Δf_{AB} and the gradual shift of absorption strength from mode B to mode A η_{AB}. Only the linewidths of the simulated mode eigenfrequencies are larger than the measured spectra because we overestimated the damping α in the calculations.

For the spectrum of rings with $w=930$ nm we find that the computed linewidth of mode B is large. One reason is certainly again that the assumed damping $\alpha=0.01$ is higher than the experimental one. But we also believe that the higher linewidth leads to a merging of closely spaced satellite peaks into the broad main peak. A detailed comparison of computed spectra for the disk and the ring with $w=930$ nm shows that the peak of mode B of the ring is broader than for the disk despite the same damping parameter α. So it is likely that the satellite which we measure at 10.5 GHz in the experiment in Fig. 4(b) is also present in the computation but becomes merged with the peak of mode B in the simulation. Figures 6(a) and 6(b) summarize the experimental and computational relative absorption strength η_{AB} and the frequency splitting Δf_{AB}, respectively.

Due to the good agreement between measured and simulated spectra we have used computed eigenmode profiles,

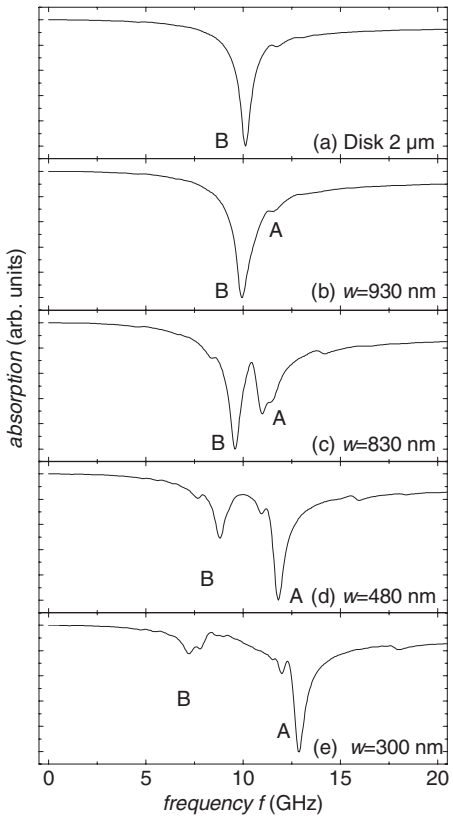

FIG. 5. Calculated absorption spectra for a disk and rings with geometrical parameters corresponding to the experimental ones (for details see text). Widths are given in each panel. The damping constant α is chosen to be 0.01.

i.e., the spatial distribution of the spin wave amplitude, to understand the systematic development of the modes. Computed eigenmode profiles for the modes A and B are presented in Fig. 7.

Before we start to discuss the individual graphs it is instructive to review general features of spin waves in micromagnets. Spin wave eigenmodes can be classified in three main categories. First, there are modes with nodes and hence finite wave vector $\boldsymbol{k}$ perpendicular to the static magnetization. They exhibit Damon-Eshbach (DE) character.[36,37] Damon-Eshbach modes obey a positive group velocity $df_{\mathrm{DE}}/dk>0$. That means that a higher wave vector causes a higher eigenfrequency. Second, there are modes with nodes and k-vector parallel to the magnetization. The modes have backward volume magnetostatic wave (BVMSW) character.[36,37] BVMSW modes have a negative group velocity $df_{\mathrm{BVMSW}}/dk<0$ below a certain wave vector k_{min} in the range $0<k<k_{\mathrm{min}}$.[37] In this range an increasing number of nodes means a decreasing eigenfrequency of the BVMSW. In general the eigenmodes will have a mixed DE and BVMSW character. Third, there exist spin-wave well modes. The "wells" are typically narrow regions at the edges of a micromagnet with a low internal field and the modes are exchange dominated.[6] The existence of all these modes has already been identified in rectangular prism shaped micromagnets.[7,51–53] They also appear in disks but are distorted to fit the curved boundary.[12]

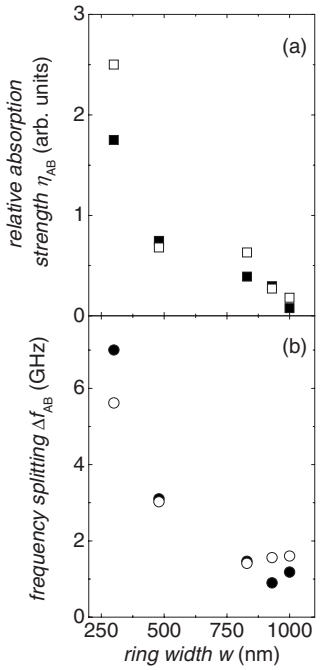

FIG. 6. Comparison of the (a) experimental and computed relative absorption strength η_{AB} and (b) the frequency splitting Δf_{AB}. Black filled symbols: Experiment, empty symbols: Computation.

We index the observed modes by the number of nodes (n,m). Here, n counts the nodes perpendicular to the magnetization and m counts the nodes along the magnetization. From Fig. 7 it is obvious that for wide rings and disks Cartesian coordinates are the more appropriate description, whereas for narrow rings cylindrical coordinates are more adequate. Note, that we use the same indices for Cartesian and cylinder coordinates. In the case of a homogeneous excitation field $\boldsymbol{h}_{\mathrm{rf}}$ one expects to excite only modes with an even number of nodes (or odd number of crests equivalently). Modes with n or m odd cannot be excited due to the vanishing odd Fourier components of the excitation magnetic field.[54]

Let us first discuss the disk and in particular the mode profile of mode B which dominates the eigenspectrum. The disk mode B is indexed by (0,0), and resembles coarsely a uniform, Kittel-like mode. Due to the applied in-plane field it has no perfect radial symmetry. The mode has a wave vector in both in-plane directions due to the confinement but is uniform otherwise. Mode A in the disk, indexed by (2,0), is a Damon-Eshbach type of mode. For the disk, the middle crest row, i.e., the row of maximum spin-wave amplitude intersecting the center of the disk, and the edge crest rows (the rows of maximum amplitude on either side of the middle crest row) have nearly the same precession amplitude and precess out of phase.

For the ring with $w=930$ nm, i.e., with small hole diameter $d=140$ nm, the mode profiles show a resemblance to disks. The inner hole introduces diagonal nodal lines in mode B. Due to these additional nodes the mode acquires a higher wave vector along the magnetization direction, and the resulting eigenfrequency is slightly lower compared to the corresponding disk mode. This was also observed in the experi-

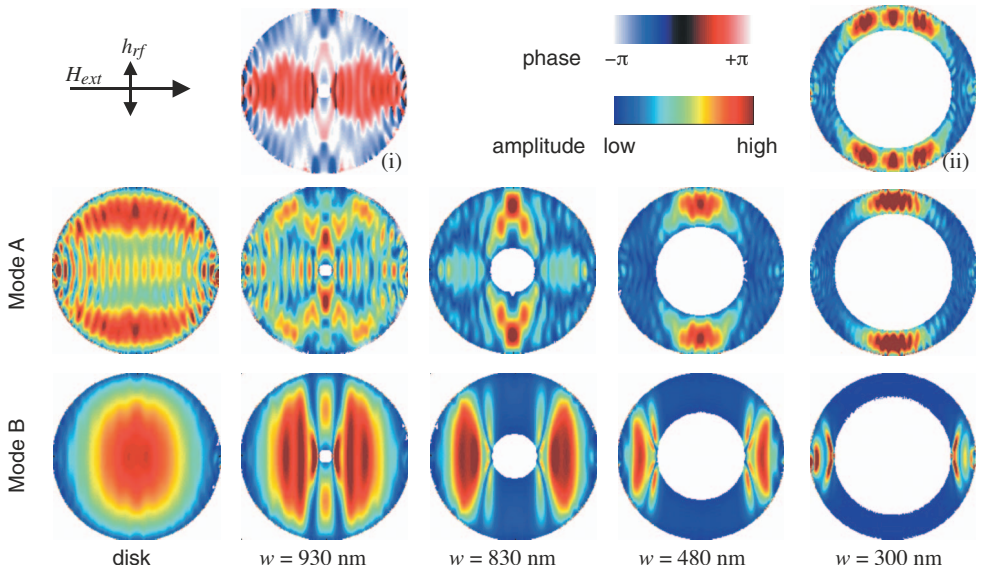

FIG. 7. (Color) Calculated mode profiles for the 2-μm-wide disk and the different ring widths as indicated at the column bottom (for details see text). In the simulation an external field of 90 mT lies along the horizontal axis. We show the mode profiles of the main modes A and B in the two bottom rows. Panel (i) on the top depicts the phase of mode A for the ring with w=930 nm and panel (ii) the satellite mode at 12.0 GHz below mode A for w=300 nm. For color coding compare the colorbar.

ment. Mode A is also influenced by the small hole but is still Damon-Eshbach-like with two nodal lines. Panel (i) depicts the phase information of mode A (compare colorbar). In this representation it becomes clear that the middle row and the edge rows precess out of phase with each other reflecting two nodal lines. In the simulations there is ripple with high spatial frequency superimposed. This is assumed to be a consequence of choosing the cell size not significantly smaller than the exchange length.[7,55]

The inner hole modifies the spectrum more severely for a ring with w=830 nm. Here, the hole diameter is 340 nm. Mode B now shows localization in the head and tail of the ring. In these portions of the ring the mode is relatively uniform. In the side arms the spin wave amplitude is vanishingly small. Mode A, which has a higher eigenfrequency than mode B, is very interesting here. It is still reminiscent of the disk mode (2,0). The edge crest rows, however, do not extend from the head to the tail anymore. A substantial contraction of the spin precession amplitude in the side arms is visible. The spin-wave amplitude in the middle crest row is very weak and vanishes completely for the narrower rings.

Rings with w=480 nm display a clear localization for both mode A and B. Here mode B, the counterpart to the disk mode (0,0), resides well confined in the ring's head and tail. Mode A, the counterpart to the disk mode (2,0) has maxima in the side arms only; the middle crest row of the spin wave excitation no longer exists at w=480 nm. As we will outline in detail later, this is due to the fact that the internal field $\boldsymbol{H}_{\mathrm{int}}(x,y)$ is spatially inhomogeneous. $\boldsymbol{H}_{\mathrm{int}}$ in the side arms and head and tail has become increasingly different as a function of increasing hole diameter. The middle crest row spins can no longer precess at the same frequency as the edge row spins in this eigenmode.

The narrowest ring (w=300 nm) follows the trend. Modes A and B are spatially separated. Mode A is found in the side arms and mode B in the head and tail. The ring segments where we find appreciable precessional amplitude are smaller than in the ring with w=480 nm. Panel (ii) in Fig. 7 shows in addition the satellite at 12.0 GHz below mode A. We find that it is localized in the same side arms as mode A but has two nodes along the azimuthal direction. Again, due to the homogeneous excitation we cannot excite modes with an odd number of nodes. Analyzing the satellite at eigenfrequency 11.6 GHz yields four nodes along the azimuthal direction (not shown). As a consequence these satellite modes are indexed by $A(2,0)$ and $A(4,0)$. "A" is introduced to avoid potential confusion with modes of type B which can exhibit the same mode indices in the case of rings. Although at first sight the spin-wave mode profiles in narrow rings have little in common with the original disk modes, our results show that they can be traced back to the disk modes (0,0) and (2,0).

IV. LOCALIZATION OF DIPOLAR MODES IN RINGS

A. Qualitative considerations

We now provide a qualitative explanation of the mode localization by addressing the observed frequency splitting Δf_{AB}. The splitting increases with decreasing width [Fig. 6(b)]. The frequency of a mode is governed by the internal field value for a particular mode and its wave vector $\boldsymbol{k}_{nm}$, therefore we have to look at both quantities in the cases of disks and rings.

In a disk the internal field $\boldsymbol{H}_{\mathrm{int}}(x,y)$ is relatively homogeneous with the exception of the edges perpendicular to the direction of the external field H_{ext}. In this case the eigenfrequencies of allowed modes are mainly determined through the value of the corresponding wave vectors. If we introduce a hole in the disk we add the inner edges to our micromagnet

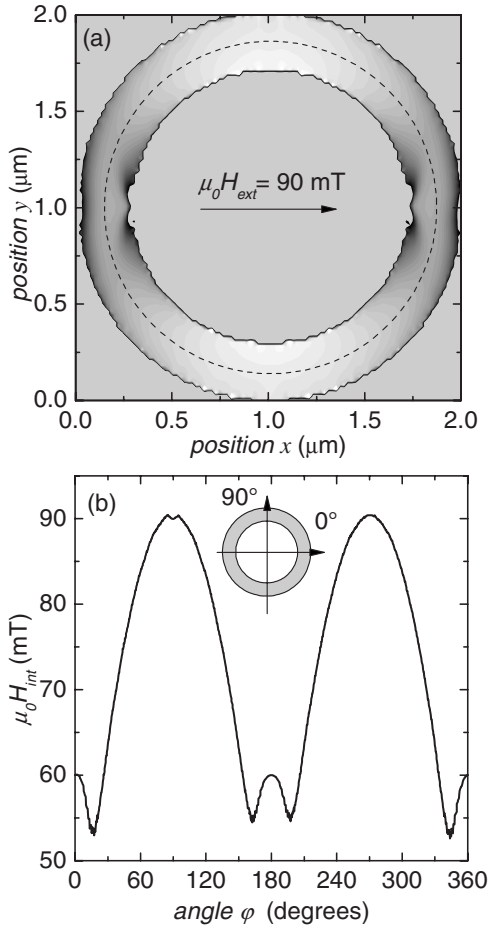

FIG. 8. (a) Micromagnetically calculated internal field profile for the 300 nm ring. White corresponds to high values grey to low values. The external field is $\mu_0 H_{\text{ext}}$=90 mT, applied in the horizontal direction. (b) Azimuthal cut of the internal field profile along the dashed line defined in (a) by $\bar{R}$ with the ring center at (1 μm, 1 μm). The angle φ is defined in the inset.

and create an internal field inhomogeneity. Figure 8(a) depicts the internal field of a ring with w=300 nm (largest inhomogeneity) in a gray-scale plot. The calculations show that the field is relatively homogeneous in the radial direction except for the domain wall region. We can therefore obtain all essential information about the internal field by looking at an azimuthal cut through the internal field $H_{\text{int}}(\bar{R},\varphi)$ with $\bar{R}=D_0/2-w/2$ fixed. In Fig. 8(b) we present such an azimuthal cut. The field inhomogeneity $\theta=(H_{\text{int}}^{\max}-H_{\text{int}}^{\min})/H_{\text{int}}^{\max}$ is as large as 30% along the azimuthal direction. Spins around 0° and 180° have a component perpendicular to the inner and outer edges and produce a demagnetizing field H_{dm}, which is oriented such that it decreases the internal field. On the other hand, where the spins are along the edges ("side arms") the internal field is only slightly decreased from the external field value. From this consideration it is consistent that mode A lies mainly in the high internal field region and mode B in the low internal field region.

Let us now turn to the wave vectors. The precessional motion of spins produces a dynamic demagnetizing field. In the side arms (φ=90°,270°) the concomitant energy penalty is minimized by effectively pinning the spins at the ring edges.[56,57] A detailed analysis of simulated spin-wave patterns in Fig. 7 reveals that modes $A(0,0)$ in the localization regime ($w \leqslant 480$ nm) do have a smaller amplitude at the side arm edges compared to the side arm centers. Although permalloy is usually considered to have negligible pinning the precession amplitude is decreased towards the edges due to the dynamic demagnetizing field. This results in a finite wave vector on the order of $k_r=\pi/w$, which increases the frequency of a spin wave in this ring segment. Combined with the large H_{int} it becomes clear that spins in the side arms must have a far higher eigenfrequency than those in the head and tail of a narrow ring.

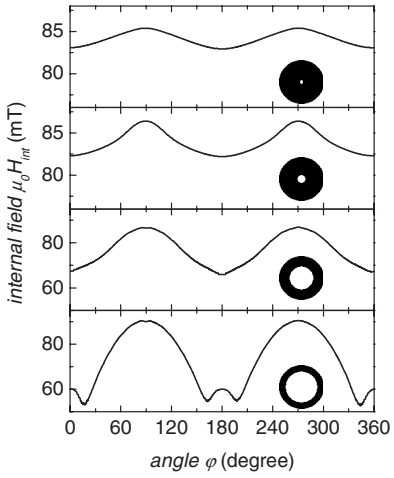

FIG. 9. Simulated internal field profiles at $\bar{R}=D_0/2-w/2$ along the azimuthal direction for the four different widths w of 930, 830, 480, and 300 nm (from top to bottom). The ring geometries are sketched in insets. Note that the H_{int} scales differ for the four rings.

The frequency splitting [Fig. 6(b)] provides important information for a microscopic understanding of the mode localization. The inner hole produces an inhomogeneity in the internal field compared to the disk. A spin wave eigenmode obviously maintains a constant frequency throughout a micromagnet, i.e., $f_{nm}(r,\varphi)$=const. When the internal field is inhomogeneous the wave vector has to change spatially to compensate for the change in internal field. In Fig. 9 we show the internal field profile along the azimuthal direction at $\bar{R}$ calculated for the ring widths of this work. (Note the different scales for the vertical axis in Fig. 9.) It is found that a decreasing ring width leads to a strong field inhomogeneity. Localization of spin waves takes place for rings where the internal field varies so much as a function of angle φ that wave vectors for an eigenfrequency become imaginary. This will be discussed quantitatively in Sec. IV.

In disks a spin wave can extend throughout the disk, because here all spins can precess at the same frequency. In rings, there is a breakup in high and low frequency segments. The mode localization occurs as soon as a constant frequency cannot be maintained in the different regions of the ring. The ring with w=830 nm is close to the transition to mode localization: mode A still extends over the ring but

with very small spin-wave amplitude in the head and tail (middle crest row). In contrast, mode B, i.e., the spin wave excitation at smaller eigenfrequency, is found to localize in the two segments of small internal field. The middle crest row of mode A and mode B are expected to have similar frequencies because they both precess in the head and tail region and have a similar wave vector. In the calculated spectrum in Fig. 5(c) there is still a frequency overlap of modes A and B. Therefore we conclude that also the middle crest row can still be driven at the eigenfrequency f_A. In narrower rings the middle crest row is no longer excited, the internal field difference between the outer crest rows and the middle crest row being too high. The localized mode A in narrow rings is thus derived from the disk (2,0) mode but the middle crest row does not exist anymore and the outer crest rows are strongly contracted.

B. Approximate mathematical treatment of narrow rings

So far we have discussed the underlying mechanism of the mode localization. We now present a semianalytical model to provide a quantitative understanding. In principle, to calculate the spin wave spectrum one would have to solve the Landau-Lifshitz equation with the full effective magnetic field[58]

$$\boldsymbol{H}_{\mathrm{eff}} = \boldsymbol{H}_{\mathrm{ext}} + \frac{2A}{\mu_0 M_S^2}\nabla^2 \boldsymbol{M} + \int_V \boldsymbol{G}(\boldsymbol{r},\boldsymbol{r}')\boldsymbol{M}(\boldsymbol{r},\boldsymbol{r}')d\boldsymbol{r}. \quad (2)$$

Here, $\boldsymbol{H}_{\mathrm{ext}}$ is the external magnetic field, the second term is the exchange field with A the exchange constant and $\boldsymbol{G}(\boldsymbol{r},\boldsymbol{r}')$ the tensorial Green's function that relates the dynamic magnetization to a dynamic demagnetizing field and the static demagnetizing field to the static magnetization. [$\boldsymbol{M}=\boldsymbol{M}_0+\boldsymbol{m}(\boldsymbol{k},t)$ contains static and dynamic parts of the magnetization.] Taking into account all field terms leads to an integrodifferential equation that can be found in similar form, for example in Ref. 51. A full-fledged analytical solution of this equation is possible only in certain cases. To achieve more insight into the problem than by using the full-micromagnetic integration of the LLG we seek for an approximate solution that still allows us to understand the mode localization.

For the semianalytic description we assume that modes can be described as plane waves with a spatially varying wave vector

$$\boldsymbol{m}(\boldsymbol{k},t) = \boldsymbol{m}_{mn}(\boldsymbol{r})\exp\{i[\boldsymbol{k}_{mn}(\boldsymbol{r})\cdot\boldsymbol{r} - \omega_{mn}t]\}. \quad (3)$$

The basic idea is thus the same as in the description of spin wave well modes,[6] spin wave modes in inhomogeneously magnetized stripes,[5,35,59,60] and closely related to the localization of dipolar spin waves in rectangular prisms.[7,51]

The angular dependence of the wave vector is extracted by noting that the frequency of a mode ω_{mn} is constant throughout the internal field profile:

$$\omega_{mn} = \omega_{mn}[\boldsymbol{H}_{\mathrm{int}}(\boldsymbol{r}),\boldsymbol{k}_{mn}(\boldsymbol{r})] = \mathrm{const}. \quad (4)$$

If the dispersion is known, then the spatially dependent wave vector can be reconstructed from the intersections of the local dispersion curves with the experimental mode frequency.[6] Note that this is mathematically analogous to the WKB approximation of a quantum mechanical wave function in a potential. The stepping stone is, of course, that one does not know the exact dispersion relation and has to resort to an approximate one.

We closely follow Guslienko *et al.*[51] and Bayer *et al.*[7] who have argued that if the aspect ratios of a magnetic element are small $t/w, t/R \ll 1$, then the dynamical dipole-dipole elements in all matrices are negligible. As a consequence one can use the dispersion of an infinite film with wave vectors whose form is dictated by the symmetry of the magnetic element under consideration. We do the same in the case of rings. The wave vectors will then be given by

$$k_{n\varphi} = \frac{(n+1)\pi}{\xi} \quad \text{and} \quad k_{m\rho} = \frac{(m+1)\pi}{w_{\mathrm{eff}}}. \quad (5)$$

Here, $\xi = \bar{R}\Phi_0$ denotes the arc length in azimuthal direction over which the mode exists and w_{eff} is the effective width of the ring as defined in Ref. 56. Using these wave vectors, the dispersion relation becomes

$$\omega_{mn}^2 = (\omega_{mn}^H + D\omega_M\kappa_{mn}^2) \times [\omega_{mn}^H + D\omega_M\kappa_{mn}^2 + \omega_M F_{mn}(\kappa_{mn}t)]. \quad (6)$$

$\kappa_{mn}^2 = k_{n\varphi}^2 + k_{m\rho}^2$ denotes the total in-plane wave vector. The inhomogeneity of the internal field is taken into account by an average of the micromagnetically calculated $H_{\mathrm{int}}(\rho,\varphi)$ weighted with the mode profile[51]

$$\omega_{mn}^H = |\gamma|\mu_0\langle H_{\mathrm{int}}\rangle_{m_{mn}} = \frac{\int H_{\mathrm{int}} m_{mn}^2 d^2r}{\int m_{mn}^2 d^2r}. \quad (7)$$

Within this approach, in principle, one must start from known mode profiles to calculate the dispersion and check the consistency. As in the case of rectangular structures we assume that a factorization is possible so that the normalized mode profiles have the form

$$m_{mn}(\rho,\varphi) = \mu(k_{m\rho},\rho)\,\eta(k_{n\varphi},\varphi). \quad (8)$$

In particular, the functions μ and η can be expressed by cosine and sine functions for even and odd indices n,m, respectively.[51] This functional form is consistent with the results of the micromagnetic simulations shown in Fig. 5 for the strongly localized modes A. Based on such assumed mode profiles, ω_{mn}^H acquires the form $\omega_{mn}^H = |\gamma|\mu_0 H - |\gamma|\mu_0\langle H_{\mathrm{dm}}\rangle_{m_{mn}}$ (see Ref. 58), with

$$\langle H_{\mathrm{dm}}\rangle_{m_{mn}} = \frac{4|\gamma|\mu_0}{\xi(R_o^2/2 - R_i^2/2)} \times \int_{R_i}^{R_o}\int_{(\pi-\Phi_0)/2}^{(\pi+\Phi_0)/2} H_{\mathrm{dm}}(\varphi) m_{mn}^2(r-\bar{R},\varphi) dr r d\varphi. \quad (9)$$

Here, R_i and R_o are the inner and outer radius, respectively,

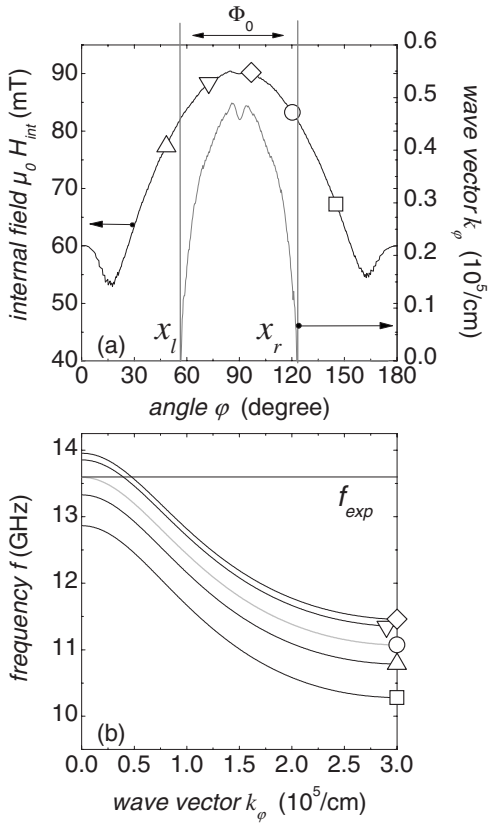

FIG. 10. (a) Micromagnetically calculated internal field profile for the ring with $w=300$ nm. The symbols ○, ▽, △, □, ◇ mark the positions at which the dispersion curves in panel (b) are calculated for mode $A(0,0)$. The grey line in (a) is the azimuthal wave vector $k_\varphi(\varphi, H_{\text{int}})$ extracted from the intersections of the calculated dispersion curves at different H_{int} in (b) with the experimental frequency. The dashed line (○) in panel (b) is the lowest-lying dispersion curve which has an intersection with at $k_\varphi \geqslant 0$. This curve defines the localization length Φ_0 along the azimuthal direction (measured in degrees).

and $\bar{R}$ is the radius at half the ring width. For completeness, the matrix element $F(\kappa_{mn}t)$ is given by[37,51]

$$F_{mn}(\kappa_{mn}t) = 1 - P(\kappa_{mn}t)\left(\frac{k_{n,\varphi}^2}{\kappa_{mn}^2}\right) + P(\kappa_{mn}t) \times [1 - P(\kappa_{mn}t)] \times \left(\frac{\omega_M}{\omega_{mn}^H + D\omega_M\kappa_{mn}^2}\right)\left(\frac{k_{m,\varphi}^2}{\kappa_{mn}^2}\right) \tag{10}$$

with

$$P(\kappa_{mn}t) = 1 - \frac{1 - \exp(-\kappa_{mn}t)}{\kappa_{mn}t}. \tag{11}$$

C. Approximate analytical results for narrow rings

We have performed the calculation outlined in the previous subsection for the case of mode A in a ring with $w=300$ nm. The result is presented in Fig. 10. In panel (a) the internal field along the azimuthal direction φ at $\bar{R}$ is reproduced for an external field of 90 mT. In panel (b) dispersion curves are displayed which are calculated for positions indicated by the markers in (a). We find that intersections with the experimental frequency exist only for dispersion curves at positions which are between the vertical grey lines (positions x_l and x_r). Here, the wave vector k_φ has a real value. Outside this ring segment wave vectors become imaginary and spin waves are exponentially damped. (Due to the symmetry of the onion state we need only look at the region of real wave vectors near $\varphi=90°$, the region around $\varphi=270°$ is identical.) The points x_l and x_r act as turning points for the localized spin wave. The distance Φ_0 between the turning points can be converted to the localization length $\xi_{(0,0)} = \bar{R}\Phi_0 \approx 1200$ nm of mode $A(0,0)$. In Fig. 11 we repeat the results from the micromagnetic calculation for modes $A(0,0)$ and $A(2,0)$ of the ring with $w=300$ nm and compare them with the mode profiles based on the approximate analytical formalism. For the ring with $w=300$ nm the LLG computation yields $\xi_{(0,0)}^C \approx 1340$ nm. Here, the turning points are taken to be the points where the amplitude has dropped to 10% of the maximum amplitude, which is also the baseline value of the computed profiles. Both values, from the LLG computation and from the WKB approach (Figs. 10 and 11, right hand column) are in good agreement. Following the WKB approach we find that the localization length of mode $A(2,0)$ is increased. We get $\xi_{(2,0)} \approx 1800$ nm. The LLG computation suggests $\xi_{(2,0)}^C = 1780$ nm. These two values are again in good agreement. The larger localization length $\xi_{(2,0)}$ is a consequence of the lower frequency of this mode.

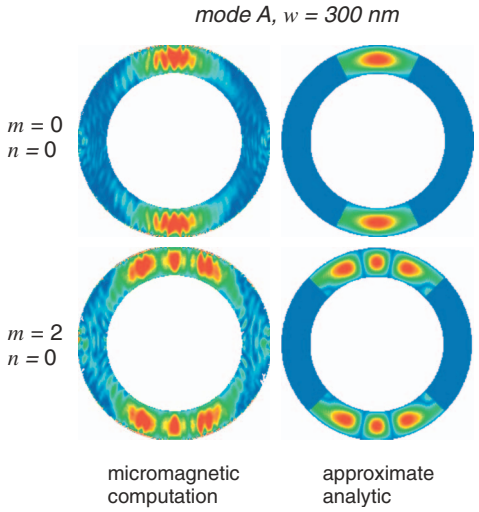

FIG. 11. (Color) Comparison of mode profiles of mode A for the $w=300$ nm ring from the micromagnetic computation (left column) and the approximate analytic mode profiles with wave vectors calculated as described in the text. For a color bar see Fig. 7. All panels are scaled such that the maximum amplitude equals 1.

The WKB approach allows one to perform a consistency check by evaluating the phase integral

$$I_n = \int_{x_l}^{x_r} k_{n\varphi}[\omega_{mn}, H_{\text{int}}(\varphi)]\bar{R}d\varphi. \quad (12)$$

The value of this integral is expected to be $I_n=(n+1)\pi$ (assuming no phase jumps at the turning points) to yield constructive self-interference. The numerical values for the modes $A(0,0)$ and $A(2,0)$ are $I_{(0,0)}=3.579$ (larger than π by 15%) and $I_{(2,0)}=12.3315$ (larger than 3π by 25%). It has been conjectured in other publications that phase jumps might occur at turning points which are not negligible.[35] The phase integral is generally considered an order-of-magnitude check.

The calculation presented in the previous section explains the mode localization of mode *A* in the side arm of a narrow ring with reasonable accuracy. The calculation is, however, not easily extended to the wider rings because "guessing" the mode profiles for the calculation is not trivial. The same holds true for the *B*-type modes in the head and tail regions. What the calculation clearly demonstrates, however, is that the inhomogeneity of the internal field is responsible for confining mode *A* in a segment of length ξ in the azimuthal direction and how in principle the localization can be understood. The part of the argumentation summarized in Eq. (4) holds true qualitatively also for mode *B* in the narrow rings: Here the spin waves are confined in the internal field minimum and an increase in the internal field away from the positions $\varphi=0,\pi$ cannot be compensated by the wave vector.

From the semianalytical approach no obvious rule of thumb can be inferred at what value w_{th} the crossover between localized and extended spin wave modes occurs. It depends on all the geometrical parameters (not only the exact width). The WKB approach, however, explains the fundamental process for mode localization qualitatively for all other localized modes and ring widths.

V. CONCLUSIONS

We have presented an experimental and theoretical study of the internal-field driven spin wave eigenmode localization transition in mesoscopic rings in the quasisaturated state. We found a systematic development of the spectra with the ring width consisting of a frequency splitting of two main modes and a gradual shift of absorption strength from one mode to the other. This observation was explained as a gradual mode localization as a function of increasing hole diameter (decreasing ring width). Up to a threshold width w_{th}, the mode profiles characteristic for disks were still recognizable in rings. Below w_{th} the modes break up in distinctly localized modes. We have applied a WKB approach, which explains the mode localization quantitatively for narrow rings. The localization results from the increasing internal field inhomogeneity.

ACKNOWLEDGMENTS

This work was financially supported by the BMBF through Grant No. 13N8283, by the DFG through SFB668 and "Nanosystems Initiative Munich (NIM)" as well as CIAR and iCore. We gratefully acknowledge D. Heitmann for his continuous support of our work and M. R. Freeman for support and the possibility to perform the dynamic micromagnetic simulations in his group at the University of Alberta.

*giesen@mbi-berlin.de
†grundler@ph.tum.de

[1] B. Hillebrands and K. Ounadjela, *Spin Dynamics in Confined Magnetic Structures I & II, Topics in Applied Physics* (Springer, Berlin, 2002).
[2] B. Hillebrands and A. Thiaville, *Spin Dynamics in Confined Magnetic Structures III, Topics in Applied Physics* (Springer, Berlin, 2006).
[3] M. Buess, R. Höllinger, T. Haug, K. Perzlmaier, U. Krey, D. Pescia, M. R. Scheinfein, D. Weiss, and C. H. Back, Phys. Rev. Lett. **93**, 077207 (2004).
[4] K. Perzlmaier, M. Buess, C. H. Back, V. E. Demidov, B. Hillebrands, and S. O. Demokritov, Phys. Rev. Lett. **94**, 057202 (2005).
[5] J. P. Park, P. Eames, D. M. Engebretson, J. Berezovsky, and P. A. Crowell, Phys. Rev. Lett. **89**, 277201 (2002).
[6] J. Jorzick, S. O. Demokritov, B. Hillebrands, M. Bailleul, C. Fermon, K. Y. Guslienko, A. N. Slavin, D. V. Berkov, and N. L. Gorn, Phys. Rev. Lett. **88**, 047204 (2002).
[7] C. Bayer, J. Jorzick, B. Hillebrands, S. O. Demokritov, R. Kouba, R. Bozinoski, A. N. Slavin, K. Y. Guslienko, D. V. Berkov, N. L. Gorn, and M. P. Kostylev, Phys. Rev. B **72**, 064427 (2005).
[8] F. Giesen, J. Podbielski, T. Korn, M. Steiner, A. van Staa, and D. Grundler, Appl. Phys. Lett. **86**, 112510 (2005).
[9] F. Giesen, J. Podbielski, T. Korn, and D. Grundler, J. Appl. Phys. **97**, 10A712 (2005).
[10] J. Podbielski, F. Giesen, and D. Grundler, Phys. Rev. Lett. **96**, 167207 (2006).
[11] I. Neudecker, M. Kläui, K. Perzlmaier, D. Backes, L. J. Heyderman, C. A. F. Vaz, J. A. C. Bland, U. Rüdiger, and C. H. Back, Phys. Rev. Lett. **96**, 057207 (2006).
[12] I. Neudecker, K. Perzlmaier, F. Hoffmann, G. Woltersdorf, M. Buess, D. Weiss, and C. H. Back, Phys. Rev. B **73**, 134426 (2006).
[13] L. Giovannini, F. Montoncello, F. Nizzoli, G. Gubbiotti, G. Carlotti, T. Okuno, T. Shinjo, and M. Grimsditch, Phys. Rev. B **70**, 172404 (2004).
[14] M. Bailleul, R. Höllinger, and C. Fermon, Phys. Rev. B **73**, 104424 (2006).
[15] M. Belov, Z. Liu, R. D. Sydora, and M. R. Freeman, Phys. Rev. B **69**, 094414 (2004).
[16] K. Buchanan, P. E. Roy, M. Grimsditch, F. Y. Fradin, K. Y. Guslienko, S. D. Bader, and V. Novosad, Nat. Phys. **1**, 172 (2005).
[17] Y. Acremann, C. H. Back, M. Buess, O. Portmann, A. Vaterlaus, D. Pescia, and H. Melchior, Science **290**, 492 (2000).
[18] W. K. Hiebert, G. E. Ballentine, and M. R. Freeman, Phys. Rev. B

65, 140404(R) (2002).
[19] W. K. Hiebert, L. Lagae, and J. DeBoeck, Phys. Rev. B **68**, 020402(R) (2003).
[20] B. C. Choi, M. Belov, W. K. Hiebert, G. E. Ballentine, and M. R. Freeman, Phys. Rev. Lett. **86**, 728 (2001).
[21] T. Gerrits, H. A. M. van den Berg, J. Hohlfeld, L. Bär, and T. Rasing, Nature (London) **481**, 509 (2002).
[22] H. W. Schumacher, C. Chappert, R. C. Sousa, P. P. Freitas, and J. Miltat, Phys. Rev. Lett. **90**, 017204 (2003).
[23] C. H. Back, R. Allensbach, W. Weber, S. S. P. Parkin, D. Weller, E. L. Garwin, and H. C. Siegmann, Science **285**, 864 (1999).
[24] M. Bauer, R. Lopusnik, J. Fassbender, and B. Hillebrands, Appl. Phys. Lett. **76**, 2758 (2000).
[25] M. R. Freeman, R. W. Hunt, and G. M. Steeves, Appl. Phys. Lett. **77**, 717 (2000).
[26] H. Shima, K. Y. Guslienko, V. Novosad, Y. Otani, K. Fukamichi, N. Kikuchi, O. Kitakami, and Y. Shimada, J. Appl. Phys. **91**, 6952 (2002).
[27] V. Novosad, K. Y. Guslienko, H. Shima, Y. Otani, S. G. Kim, K. Fukamichi, N. Kikuchi, O. Kitakami, and Y. Shimada, Phys. Rev. B **65**, 060402(R) (2002).
[28] R. P. Cowburn, Phys. Rev. B **65**, 092409 (2002).
[29] C. Mathieu *et al.*, Appl. Phys. Lett. **70**, 2912 (1997).
[30] S. P. Li, D. Peyrade, M. Natali, A. Lebib, Y. Chen, U. Ebels, L. D. Buda, and K. Ounadjela, Phys. Rev. Lett. **86**, 1102 (2001).
[31] J. Rothman, M. Kläui, L. Lopez-Diaz, C. A. F. Vaz, A. Bleloch, J. A. C. Bland, Z. Cui, and R. Speaks, Phys. Rev. Lett. **86**, 1098 (2001).
[32] X. Zhu, M. Malac, Z. Liu, H. Qian, V. Metlushko, and M. R. Freeman, Appl. Phys. Lett. **86**, 262502 (2005).
[33] F. Giesen, J. Podbielski, B. Botters, and D. Grundler, Phys. Rev. B **75**, 184428 (2007).
[34] C. Mathieu, J. Jorzick, A. Frank, S. O. Demokritov, A. N. Slavin, B. Hillebrands, B. Bartenlian, C. Chappert, D. Decanini, F. Rousseaux, and E. Cambril, Phys. Rev. Lett. **81**, 3968 (1998).
[35] C. Bayer, S. O. Demokritov, B. Hillebrands, and A. N. Slavin, Appl. Phys. Lett. **82**, 1607 (2003).
[36] R. W. Damon and J. R. Eshbach, J. Phys. Chem. Solids **19**, 308 (1961).
[37] B. A. Kalinikos and A. N. Slavin, J. Phys. C **19**, 7013 (1986).
[38] A. N. Slavin, *Spin Waves in Confined Magnetic Structures I*, No. 83 in Topics in Applied Physics (Springer, Berlin, 2002), Chap. 2, p. 34.
[39] S. O. Demokritov, V. E. Demidov, O. Dzyapko, G. A. Melkov, A. A. Serga, B. Hillebrands, and A. N. Slavin, Nature (London) **443**, 430 (2006).
[40] M. Bailleul, R. Höllinger, and C. Fermon (unpublished).
[41] J. D. Jackson, *Classical Electrodynamics*, 3rd ed. (Wiley, New York, 1998).
[42] T. J. Silva, C. S. Lee, T. M. Crawford, and C. T. Rogers, J. Appl. Phys. **85**, 7849 (1999).
[43] T. M. Crawford, M. Covington, and G. J. Parker, Phys. Rev. B **67**, 024411 (2003).
[44] D. Chumakov, J. McCord, R. Schäfer, L. Schultz, H. Vinzelberg, R. Kaltofen, and I. Mönch, Phys. Rev. B **71**, 014410 (2005).
[45] Sonnet Lite, http://www.sonnetusa.com/products/lite/
[46] I. Neudecker, G. Woltersdorf, B. Heinrich, T. Okuno, G. Gubbiotti, and C. H. Back, J. Magn. Magn. Mater. **307**, 148 (2006).
[47] M. Covington, T. M. Crawford, and G. J. Parker, Phys. Rev. Lett. **89**, 237202 (2002).
[48] M. R. Scheinfein, LLG Micromagnetics Simulator, http://llgmicro.home.mindspring.com
[49] F. Giesen, Ph.D. thesis, Institut für Angewandte Physik, Universität Hamburg, Germany, 2005.
[50] M. J. Donahue and D. G. Porter, OOMMF User's Guide, Version 1.0, Interagency Report NISTIR 6376, National Institute of Standards and Technology, Gaithersburg, MD, 1999.
[51] K. Y. Guslienko, R. W. Chantrell, and A. N. Slavin, Phys. Rev. B **68**, 024422 (2000).
[52] K. Y. Guslienko and A. N. Slavin, J. Appl. Phys. **87**, 6337 (2000).
[53] S. Tamaru, J. A. Bain, R. J. M. van de Veerdonk, T. M. Crawford, M. Covington, and M. H. Kryder, J. Appl. Phys. **91**, 8034 (2002).
[54] C. Kittel, Phys. Rev. **110**, 1295 (1958).
[55] Due to the nonmonotonous dispersion of BVMSW modes there are pairs of frequency degenerate k vectors on either side of the frequency minimum at $k_{\min}$. Eigenmodes belonging to both k vectors show up in the calculated mode profiles if the exchange penalty for the high k vector mode is not high enough to suppress it. Note, that the high-k ripple lies always along the magnetization, confirming the BVMSW character of the spin wave. The ripple is also seen in the other simulations but it is much less pronounced. It is hard to tell whether the high-k modes are also excited in the experiment.
[56] K. Y. Guslienko, S. O. Demokritov, B. Hillebrands, and A. N. Slavin, Phys. Rev. B **66**, 132402 (2002).
[57] K. Y. Guslienko and A. N. Slavin, Phys. Rev. B **72**, 014463 (2005).
[58] A clarification is in order for the use of the terms effective and internal magnetic field. We use effective field H_{eff} for the field that has to be inserted in the LLG, including all dynamic magnetic field terms. The term internal field H_{int} is used to denote the sum of all static field terms that are present in a ferromagnetic element, excluding the exchange field. In the absence of crystalline anisotropy the internal field reduces to the demagnetizing field H_{dm}.
[59] E. Schlömann and R. I. Joseph, J. Appl. Phys. **35**, 167 (1964).
[60] C. Bayer, J. P. Park, H. Wang, M. Yan, C. E. Campbell, and P. A. Crowell, Phys. Rev. B **69**, 134401 (2004).